

Investigation of the Stress-induced Microcracking Processes in Crystalline Rocks through Simultaneous Acoustic Emission and Strain Monitoring

Sana Zafar¹, Ahmadreza Hedayat¹, and Omid Moradian²

¹Colorado School of Mines

²ETH Zürich

November 26, 2022

Abstract

We performed laboratory-scale experiments on Barre granite specimen with a single pre-existing flaw to study the microscopic processes that occur during the deformation of a brittle material such as granite at different stress levels from crack initiation to the failure of the specimen. Here, we focus on the evolution of the tensile and shear cracks as a function of stress under unconfined compression. Acoustic emission technique (AET) in combination with the two dimensional (2-D) digital image correlation (DIC) technique have been used to track the changes in the source mechanisms of the registered AE events, along with the development of strains around the flaw tips of a uniaxially loaded prismatic Barre granite specimen. The parametric analysis along with the moment tensor inversion of the AE signals were used to discuss the cracking levels and the cracking mechanisms. In particular, the microcracks observed through AE monitoring prior to specimen failure were presented in terms of their spatio-temporal evolution and linked with the changes in the inelastic strain component measured through the 2D-DIC along the localized area. The mode of deformation computed from the image based strain profiles, enabled direct comparison of the nucleation, growth and interaction of the microcracks with the AE monitoring technique.

1 **Investigation of the Stress-induced Microcracking**
2 **Processes in Crystalline Rocks through Simultaneous**
3 **Acoustic Emission and Strain Monitoring**

4 **Sana Zafar¹, Ahmadreza Hedayat¹, Omid Moradian²**

5 ¹Department of Civil and Environmental Engineering, Colorado School of Mines, Golden, CO, USA

6 ²Department of Earth Science, Swiss Federal Institute of Technology (ETH), Zurich, Switzerland

7 **Key Points:**

- 8 • Damage evolution was continuously observed under unconfined compression on
9 prismatic Barre granite specimens.
10 • Mode of deformation observed through AE was explicitly correlated by the nonelas-
11 tic component of DIC strain
12 • Mode of deformation obtained through AE and DIC showed a consistent near-linear
13 correlation with increasing levels of stress.

Corresponding author: S. Zafar, sanazafar@mymail.mines.edu

14 Abstract

15 We performed laboratory-scale experiments on Barre granite specimen with a single pre-
16 existing flaw to study the microscopic processes that occur during the deformation of a
17 brittle material such as granite at different stress levels from crack initiation to the failure
18 of the specimen. Here, we focus on the evolution of the tensile and shear cracks as a function
19 of stress under unconfined compression. Acoustic emission technique (AET) in combination
20 with the two dimensional (2-D) digital image correlation (DIC) technique have been used
21 to track the changes in the source mechanisms of the registered AE events, along with the
22 development of strains around the flaw tips of a uniaxially loaded prismatic Barre granite
23 specimen. The parametric analysis along with the moment tensor inversion of the AE
24 signals were used to discuss the cracking levels and the cracking mechanisms. In particular,
25 the microcracks observed through AE monitoring prior to specimen failure were presented
26 in terms of their spatio-temporal evolution and linked with the changes in the inelastic
27 strain component measured through the 2D-DIC along the localized area. The mode of
28 deformation computed from the image based strain profiles, enabled direct comparison of
29 the nucleation, growth and interaction of the microcracks with the AE monitoring technique.

30 1 Introduction

31 Cracking processes in rocks is a complex phenomena. Discrete creation and propagation
32 of microcrack causes the brittle failure of the rocks. Therefore an understanding of the
33 mechanics and mechanisms involved during rock fracture plays an important role in de-
34 signing civil engineering structures and different rock breaking processes such as hydraulic
35 fracturing, drilling, and blasting etc (Z. T. Bieniawski, 1967). The microcracking processes
36 that eventually causes the failure of a material has been studied through fracture mechanics
37 which states that microcracks are created due to localized stress concentration caused by
38 the presence of pre-existing flaws. Griffith (1921) satisfactorily explained that the actual
39 stress needed to fracture a bulk material is less than the theoretical stress required to break
40 the atomic bonds of the material, this low fracture strength is due to the presence of a large
41 number of randomly distributed microscopic flaws in the material (Griffith, 1921; Z. Bieni-
42 awski, 1967). Similarly, McClintock and Irwin (McClintock & Irwin, 1965) showed that the
43 material deforms inelastically before the crack propagation due to the displacement field
44 around the tips of the pre-existing flaw known as the fracture process zone. The process
45 zone consists of microcracks and with the increase in the load, these microcracks propagate
46 and coalesce to form macrocracks which leads to the failure of the material (Wawersik &
47 Fairhurst, 1970). These studies indicate that the presence of pre-existing flaw in a material
48 acts as a stress concentrator and the growth of the microcracks particularly from these stress
49 concentration areas causes the brittle fracture of the rock specimen (S. Peng & Johnson,
50 1972; Tapponnier & Brace, 1976; Kranz, 1983). Therefore, a better understanding of the
51 cracking mechanisms involved in rock damage around a pre-existing flaw is an essential pre-
52 requisite to predict the macroscopic failure of the rock bearing structures. Although several
53 studies have been done on rock and rock-like specimens with an existing flaw by different
54 researchers (Bazant & Kazemi, 1990; Fortin et al., 2009; L. Wong & Einstein, 2009; Tal
55 et al., 2016; Li & Einstein, 2017), only limited knowledge about its fracture process under
56 unconfined compression has been obtained.

57 In order to study the evolution of microcracks in stressed rock specimen various direct
58 microstructural observation techniques such as scanning electron microscope and optical
59 microscope have been used (Brace et al., 1966; Reches & Lockner, 1994; Kranz, 1979).
60 Tapponnier and Brace (1976) investigated the progression of damage in Westerly granite
61 specimens using scanning electron microscopy (SEM) analysis. The cracking processes and
62 the increase in the crack density was observed as a function of stress. In their study, the
63 evolution of shear cracks at microscopic level was overlooked because of the low magnifica-
64 tion of the SEM. Fredrich et al. (1989) studied the micromechanical process of the brittle

65 to plastic transition in Carrara marble using optical and transmission electron microscopy
66 (Fredrich et al., 1989). Zhao et al.,(1993) characterized the different stress-induced cracking
67 mechanisms by conducting real-time SEM observations on a marble plate with an inclined
68 pre-existing flaw (Zhao et al., 1993). They observed that the microcracks were mostly ten-
69 sile in nature, with a few shear cracks (L. N. Y. Wong & Xiong, 2018). Wong and Einstien
70 (2009) performed microscopic observations on double flawed specimen under uniaxial com-
71 pression. They utilized the environmental scanning electron (ESEM) and SEM imaging
72 techniques to study the microscopic behavior and further linked the microscopic damage
73 to the macroscopic failure of the rock specimen. As per their observation, the coalescence
74 between the two pre-existing flaws took place through the evolution of a number of tensile
75 microcracks . Cheng et al. (2018) investigated the progression of damage in marble speci-
76 men containing en echelon flaws using an optical microscope. Their study investigated the
77 development of tensile and shear cracks at the microscopic and the macroscopic scale as a
78 function of stress (Y. Cheng & Wong, 2018). Although these techniques provided useful in-
79 formation about the internal microstructure of the rock material subjected to loading, they
80 failed to provide a continuous observations of the cracking processes without pausing the
81 load or interfering with the loading process (Chang & Lee, 2004; Paterson & Wong, 2005).
82 Therefore, as a continuous measurement technique, acoustic emission (AE) monitoring in
83 combination with the 2D-digital image correlation (DIC) was used in this study to analyze
84 the damage processes in real time (Moore & Lockner, 1995; Crider, 2015; Moradian et al.,
85 2016; Ghamgosar et al., 2017; Tarokh et al., 2017). The AE technique is considered as one
86 of the most widely used methods for non-destructive monitoring (Guo et al., 2017; Hampton
87 et al., 2018; Xu & Zhang, 2018; Lin et al., 2019) because of its ability to detect the dynamic
88 motions in the material whereas most of the other methods like ultrasonic testing have the
89 ability to detect the existing geometrical defects. The 2D-DIC is also the most extensively
90 used non-contact optical method for displacement and strain field measurement in real-time
91 (Pan et al., 2009; Hedayat et al., 2014; Sutton et al., 2009; Shirole et al., 2019).

92 Various experimental studies have been conducted over the past few years using the AE
93 and 2D-DIC techniques in combination for the damage characterization in rocks of various
94 geometries under different loading conditions (Lin & Labuz, 2013; Lin et al., 2014; Kao et
95 al., 2016; Guo et al., 2017; Dong et al., 2017; J.-L. Cheng et al., 2017; Li & Einstein, 2017;
96 Lin et al., 2019). Based on these researches, it can be concluded that both the techniques
97 in combination have the capability of detecting the damage initiation and evolution in the
98 rock specimen. AE detects the source location and mechanism of the AE events while DIC
99 provides the strain field related to the deformation of the material. Hence, the combination
100 of AE and DIC can provide a detailed evaluation of the fracturing process in rocks from
101 microscopic to macroscopic scale. Lin and Labuz(2013), Lin et al.(2014), Zhang et al.(2015)
102 and Lin and Labuz(2019) all adopted the above-mentioned techniques to study the fracture
103 process zone in a three point bending test on a pre-notched rock specimen. They used
104 the two techniques to identify the size of the fracture process zone at the tips of the notch
105 and to distinguish the regions accommodated with the process zone and the actual crack
106 propagation within the rock specimen. Kao et al. (2016) characterized the spalling near a
107 free surface in laboratory experiments on rocks using AE and DIC (Kao et al., 2016). They
108 analyzed the damage based on the AE locations and compared it with the inelastic strain
109 measurements obtained through DIC. However, the cracking mechanism was not studied
110 in their work. Li and Einstien, 2017 conducted four point bending experiments on a pre-
111 notched granite specimen to observe the process zone development and crack propagation
112 using AE and DIC techniques. Based on their observations they defined the extent of process
113 zone and crack front. In most of these studies on rocks the major focus was to identify the
114 damage zones based on AE source locations and the DIC strain and displacement field
115 measurements. However the evaluation of the mode of deformation from the two techniques
116 and their correlation has been rarely reported.

117 This study attempts to provide an insight into the stress-induced cracking processes involved
118 during deformation of brittle rock specimen containing a pre-existing flaw through extending

119 the available experimental observations. In this study, the cracking processes were monitored
 120 simultaneously with an 8 channel acoustic emission system and 2D-digital image correlation
 121 technique under unconfined compression. The experimental observation based on cumulative
 122 AE hits and cumulative AE energy helped to analyze the stress thresholds corresponding
 123 to different stages of cracking and the moment tensor analysis of the AE sources provided
 124 in-depth knowledge about the cracking processes involved during this period. The 2D-DIC
 125 strain measurement approach was used to monitor the evolution of damage in terms of the
 126 nonelastic strain component with increasing levels of stress. One of the new major finding
 127 of the present study was to obtain the mode of deformation from the DIC strain profiles and
 128 relate it with the cracking mechanisms obtained through the moment tensors of AE in real
 129 time. Independent measurements of tensile and shear deformation with increasing levels of
 130 loading from the two techniques provided a unique opportunity to correlate the changes in
 131 the cracking processes explicitly with the damage in the rock specimen.

132 2 Experimental Design

133 2.1 Material

134 This study for the characterization of the damage process was performed on Barre granite
 135 (BG) specimen with a single pre-existing flaw. BG is crystalline in nature and obtained
 136 from the south-west region of Burlington, Vermont (USA) (Nasseri et al., 2010; Iqbal &
 137 Mohanty, 2007). This rock is a representative of the Earth's crust and one of the most
 138 extensively studied rocks with a rich literature (e.g.,(Goldsmith et al., 1976; S. S. Peng,
 139 1975; Kranz, 1979; Morgan et al., 2013; Moradian et al., 2016)). BG is a gray granodiorite
 140 with its grain size ranging from 0.2mm to 3.0mm (medium-fine grained). It has an average
 141 grain size of 0.87mm (Nasseri et al., 2010; Iqbal & Mohanty, 2007). BG has a very consistent
 142 mineral composition which consists of about 65% feldspar (average grain size of 0.95), 27%
 143 quartz (average grain size of 0.94mm), 9% biotite (average grain size of 0.83mm) (Iqbal &
 144 Mohanty, 2007; Nasseri et al., 2010; Dai & Xia, 2010) . It has a density of 2.66 gm/cm³with
 145 a porosity of 0.59% (Iqbal & Mohanty, 2007). Barre granite specimen in its intact form has
 146 the following average properties: Young's modulus=58 GPa (Shirole, Walton, & Hedayat,
 147 2020), uniaxial compressive strength=170 MPa (Zafar et al., 2020), average compressional
 148 P- wave velocity= 4000 m/s (Moradian et al., 2016). Same block of Barre granite was used
 149 to prepare the prismatic specimens (152 mm x 76 mm x 25 mm) and the pre-existing flaws
 150 were cut by OMAX water jet. The flaw was cut throughout the thickness of the specimen.
 151 The flaw length and the its inclination angle with respect to the horizontal axis is 25mm
 152 and 45°, respectively (Figure 1a). For the purpose of experimental result presentation, three
 153 representative specimens labelled as 'BG-1', 'BG-2' and 'BG-3' are discussed in this paper
 154 from a comprehensive series of tests.

155 2.2 Loading System Set-up

156 A computer-controlled servo-hydraulic loading machine was used for conducting unconfined
 157 compression experiments on three Barre granite specimen with an existing flaw. The loading
 158 was applied in displacement controlled mode at a displacement rate of 1 $\mu\text{m/s}$. The dis-
 159 placement was controlled through three Linear Variable Differential Transformers (LVDTs).
 160 These LVDTs recorded the overall axial deformation of the rock specimen. The displacement
 161 control mode helped in controlling the deformation of the rock specimen closed to their uni-
 162 axial compressive strength to protect the AE sensors from damage. Proper synchronization
 163 was ensured among the three systems during the test.

2.3 2D-DIC Setup

Digital image correlation (DIC) technique is the most commonly used and widely accepted non-destructive, non-contacting optical deformation and strain measurement approach that can be utilized for the evaluation of the complex behavior of geomaterials (Pan et al., 2009; Hedayat et al., 2014; Sutton et al., 2009; Bruck et al., 1989). This technique evaluates full-field displacement and full-field strains to sub-pixel accuracy by comparing the reference image (without mechanical loading) to the image corresponding to strained state (under mechanical loading). Because of its sub-pixel resolution, accurate DIC measurements detect optically invisible cracks. The 2D-DIC technique is preferred over other optical methods because of its simple experimental set-up and specimen preparation and also provides accurate displacement and strain field measurement (Hedayat & Walton, 2017).

In 2D-DIC, the image taken before applying the load is known as the reference image and this reference image is then used for comparing the images acquired throughout the loading. In order to compare the images acquired in the stressed state with the reference image, the specimen surface should have a unique random gray intensity pattern. After acquiring the digital images, DIC uses a correlation function between the images, to compare the acquired image with the reference image. An area of interest (AOI) is first specified within the image and further divided into small group of pixels known as subsets (Schwartz et al., 2013). These subsets are separated from each other through the step size. In 2D-DIC, the correlation functions such as zero normalized cross-correlation (ZNCCD) or zero normalized sum of squared difference (ZNSSD) (Pan et al., 2009) is used for tracking the subsets between the reference and the deformed images. The reason behind the selection of a square subset over a single pixel is that it provides a wider variation in the intensity of the gray scale values which makes it more identifiable from other subsets in the deformed image. To get the accurate measurement in 2D-DIC and to track the changes in the reference and the deformed images, each subset is defined by a unique distribution of gray-scale values known as the speckle pattern. The 2D-DIC technique locates the subsets in the deformed image, initially defined in the reference image assuming that the gray-scale values in the subset remains preserved even after the deformation (Bourcier et al., 2013). A correlation algorithm is then implemented between the subsets of the reference and the deformed images to find the optimal matching between the coordinates. The coordinates of the extremum position of the correlation coefficient defines the new position of the deformed subset with respect to the reference subset. The difference between the position of the reference subset and the deformed subset gives the displacement vector (Hedayat et al., 2014). The procedure is then repeated for all the virtual grid lines in a systematic manner to obtain the displacement along the surface of the specimen at various stages of deformations. The numerical differentiation of the displacement field along the specimen surface gives the strain field measurement in real time. The strain field calculation is based on the standard Lagrangian approach of the continuum mechanics. The strains around the grid points are averaged across an area (filter size) to get a continuous strain profile along the surface of the specimen.

The proper implementation of the DIC technique comprises of three consecutive steps: (i) specimen preparation and experimental set-up, (ii) image acquisition, and (iii) processing the acquired images using correlation algorithm. To obtain a high-quality gray-scale distribution for accurate DIC measurements, the planar surface of the specimen was cleaned and a unique random speckle pattern was created by using a multi-color paint (Rust-Oleum) to paint the surface of the specimen (Sutton et al., 2009).

Grasshopper (Point Grey) charged coupled device (CCD) camera with a Fujinon lens of focal length 35mm was used for acquiring the digital images. The aperture, focus and polarization of the lens were operated manually. The Fly Capture SDK software was used to control the field of view from the camera, brightness, and the rate of image acquisition (Shirole et al., 2019). Before each test, dust on the polarizing lens and reflections on the surface specimen were minimized. In our experimental setup, the CCD camera was kept at a distance of 1000 mm from the planar surface of the specimen to avoid the error due to

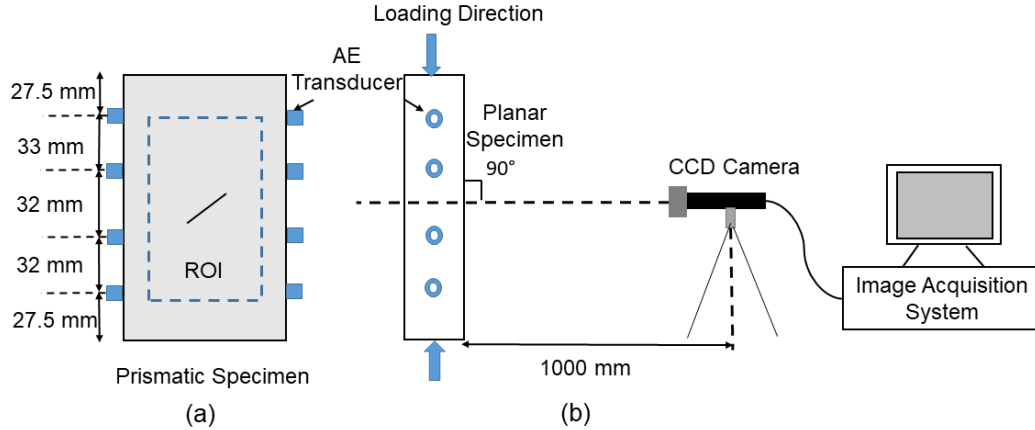


Figure 1. Schematic diagram of the (a) Prismatic specimen with a pre-existing flaw (flaw length is 25mm and the flaw inclination angle with respect to the horizontal axis is 45°) with the location of the AE sensors, the dashed blue line shows the region of interest, (B) 2D-DIC setup with the CCD camera and the image acquisition system

217 the out of plane deformations below the prescribed limit of $\Delta z/z_c \sim 10^{-4}$ (Modiriasari et al.,
 218 2017). The surface of the specimen was kept perpendicular to the optical axis of the camera
 219 and the plane of the camera parallel to the planar surface of the specimen. The images were
 220 captured at a rate of 10 frames per second for these experiments. A polarizing lens with a
 221 conjugate polarizer was used for better illumination. The DIC component of the setup is
 222 shown in Figure 1. The whole surface ($152 \times 76 \text{ mm}^2$) of the specimen was imaged with the
 223 camera.

224 The digital images captured during the experiments were analyzed using the VIC-2D soft-
 225 ware licensed by Correlated Solutions to extract the displacement and strain along the
 226 specimen surface using the correlation criterion. The analysis in the software requires the
 227 selection of the appropriate region of interest (ROI) in the reference image (Figure 1). For
 228 DIC measurements a virtual grid is formed on the reference image, which requires subset
 229 size and step size as an input to the software. According to previous research, (Hedayat
 230 et al., 2014; Shirole et al., 2019), a step size of 5 pixels and a subset size of 15 pixels were
 231 selected. This provided sufficient overlap between the subsets and required less computa-
 232 tion time for the image analysis. The correlation procedure was executed by applying a
 233 constant magnification factor to convert the pixels to their respective physical dimensions
 234 (Hedayat et al., 2014; Shirole et al., 2019). In these experiments, by comparing the pixel
 235 measurements from the fixed field of view of the camera to the physical dimension of the
 236 entire specimen surface, a constant magnification factor of $90 \mu\text{m}/\text{pixel}$ was used that is each
 237 pixel in the digital image is equal to $90 \mu\text{m}$ in the physical dimension.

238 2.4 AE Setup

239 Acoustic Emission (AE) was implemented to track the spatiotemporal changes in the reg-
 240 istered AE events around the flaw tips of the uniaxially loaded prismatic specimen. The
 241 experiment was instrumented with eight piezoelectric AE sensors mounted on the sides of
 242 the specimen (Figure 1a). The piezoelectric sensors Nano 30 from Mistras Group, Inc. were
 243 used in the study to record the AE signals. The Nano-30 AE sensor has a frequency response
 244 over the range of 125-750kHz with a resonant frequency of 300kHz. The miniature size of
 245 the sensor makes it easy to mount in small and tight spaces. They were attached on the

246 sides along the longitudinal axis of the specimen with epoxy (produced by Hardman, Royal
 247 Adhesives and Sealants). The epoxy was in contact with the sensor for 9 hours and the
 248 velocity measured by Pencil Lead Break test was documented after every 1.5 hour interval.
 249 The efficiency of the coupling was verified by the pencil lead break (PLB) and the auto
 250 sensor test (AST).

251 In this experimental-setup, 2/4/6 PAC preamplifiers were used to amplify the output voltage
 252 of the AE sensors by 20dB in order to improve the detection efficiency of the sensors for
 253 recording. The sampling frequency was 5 MHz with a sample length of 15k and a pre-trigger
 254 of 256 μ s. Eight channel board and system from the MISTRAS Group, Inc. was used as a
 255 part of the AE data acquisition system. The system was controlled by real-time operating
 256 software AEwin where the peak definition time (PDT), hit definition time (HDT) and hit
 257 lockout time (HLT) were set as 200, 800 and 350 μ s, respectively. The maximum duration
 258 was taken as 3ms.

259 All the AE signals (waveforms) were recorded and further analyzed for the source localization
 260 and source type characterization using the moment tensor inversion method reported in Li et
 261 al.(2019)(Li et al., 2019). The source location was based on the first arrival of the P-waves.
 262 The arrival time picking was done using the Akaike information criterion (AIC) (Maeda,
 263 1985; Kurz et al., 2005). Locations were determined using a constant P-wave velocity
 264 field model for a minimum distance error of 3 mm and optimized using “fmincon” function
 265 in MATLAB. While AE source location analysis helped to describe the spatiotemporal
 266 evolution of damage, AE source mechanism analysis and their dependence on the stress
 267 state of rocks enables detailed insight into the cracking processes at the microlevel.

A generalized relationship between the seismic sources and the elastic waves is summarized
 by (Richards & Aki, 1980; Ohtsu, 1991). Thus, the AE waves can be represented by

$$u_{ix,t} = G_{ip,q}(x, y, t)m_{pq} * S(t) \quad (1)$$

268 where $u_{ix,t}$ is the displacement at crack location x , $G_{ip,q}(x,y,t)$ is the spatial derivative
 269 of Green’s function, which describes the response of the medium to a disturbance, m is
 270 the moment tensor, the asterisk denotes the convolution operation and $S(t)$ represents the
 271 source time function. The moment tensor inversion analysis based on Simplified Green’s
 272 function for Moment tensor Analysis (SiGMA) procedure (Ohtsu, 1995) was used to identify
 273 the source mechanism and their evolution in these experiments. This method selects the
 274 compressional (P) wave portion from the full-space Green’s function when applied to an
 275 isotropic and homogeneous material. It is a quantitative approach in which the source is
 276 represented by a moment tensor matrix (m) (Eq. 1) which is a 3x3 matrix. The elements
 277 of the matrix describes the forces acting on the source (Graham et al., 2010). Each element
 278 in the matrix denotes one of the 9 double-couples acting at the source. Since the matrix is
 279 symmetric, it contains six independent elements. The diagonal elements represent tensile or
 280 compressional couples and the off diagonal elements represent the shear couples. The SiGMA
 281 procedure uses the simplified form of Eq.(1) to determine the six independent components of
 282 the moment tensor by solving a set of linear equations in terms of the first motion amplitude
 283 $A(x)$ as shown in Eq.(2), as follows:

$$A(x) = \frac{C_s Re(t, r)}{R} [r_1 \ r_2 \ r_3] \begin{bmatrix} m_{11} & m_{12} & m_{13} \\ m_{21} & m_{22} & m_{23} \\ m_{31} & m_{32} & m_{33} \end{bmatrix} \begin{bmatrix} r_1 \\ r_2 \\ r_3 \end{bmatrix} \quad (2)$$

284 where $A(x)$ is the amplitude of the first motion observed at the sensor location x . C_s is the
 285 coefficient of calibration for the sensor, R is the distance from the sensor to the AE source.
 286 Vector r is the direction vector of R and $Re(t,r)$ denotes the reflection coefficient (Ohtsu,
 287 1995). These values can be obtained through the source localization. Thus, source location
 288 is required to perform the moment tensor analysis.

Once the moment tensor of a source has been determined, the cracking mechanism is classified using the eigenvalues of the moment tensor (Ohtsu, 1991). The moment tensor is decomposed to its eigenvalues to split the tensor into an isotropic component (ISO), a deviatoric component 'Compensated Linear Vector Dipole' (CLVD) and a double-couple (DC) component. X and Y denotes the maximum shear and CLVD components respectively, giving a DC part (X,0,-X), a CLVD part (Y,-0.5Y,-0.5Y) and the isotropic part in direction, Z. The values of X,Y and Z calculated from the following equations are used to determine the shear and tensile crack ratios:

$$\begin{aligned}\frac{\lambda_1}{\lambda_1} &= X + Y + Z \\ \frac{\lambda_2}{\lambda_1} &= 0 - \frac{Y}{2} + Z \\ \frac{\lambda_3}{\lambda_1} &= -X - \frac{Y}{2} + Z\end{aligned}\quad (3)$$

289 where λ_1 , λ_2 and λ_3 are the maximum, intermediate and minimum eigenvalues. In the
290 SiGMA procedure, the values of X, Y and Z gives the shear, deviatoric and isotropic com-
291 ponent of the source, respectively. An AE source with $X < 40\%$ and $Y+Z > 60\%$ is classified
292 as a tensile crack, $X < 40\%$ is typically considered as a shear crack and $40\% < X < 60\%$ is
293 classified as a mixed mode crack (Ohtsu, 1995).

294 From the eigenvalue analysis of the moment tensor, three eigenvectors e_1 , e_2 , e_3 can also
295 be obtained. The eigenvector analysis of the moment tensor provides the orientation of the
296 cracks. l and n represents the cracking motion vector and the vector normal to the crack
297 surfaces which can be evaluated using equation (4):

$$\begin{aligned}e_1 &= l + n \\ e_2 &= l \times n \\ e_3 &= l - n\end{aligned}\quad (4)$$

298 In case of a tensile crack, the cracking motion vector l is parallel to the normal vector n and
299 for shear cracks the two vectors are usually perpendicular.

300 In this study, the above procedure was used not only to classify the different AE events as
301 shear, tensile, or mixed mode crack but also to identify their orientation at different levels
302 of cracking. As for the source localization in three dimensions, there are four unknowns
303 (x , y , z , and t) which require the detection of the AE signals by minimum of four channels
304 but the moment tensor has six independent components. Hence, in these experiments, the
305 source localization was also done for a minimum of six channels.

306 **3 Results and Discussion**

307 **3.1 Crack Initiation (CI) and Crack Damage (CD)**

308 Brittle rock is a heterogeneous material made up of various inherent microstructures. Nu-
309 merous experimental results demonstrate that the microcracking in rock is effected by these
310 internal heterogeneities (Brace et al., 1966; Martin & Chandler, 1994; Eberhardt et al.,
311 1998). Considering the fact that Barre granite is a brittle rock (quartz content is 27%) and
312 hence the failure is caused by the initiation, growth and coalescence of microcracks created
313 due to material heterogeneity under compression. Direct observation of these microcracks
314 have revealed that the primary mechanism of deformation in brittle rocks is local tensile
315 cracking which is due to the extensile strains (Lajtai, 1974; Tapponnier & Brace, 1976;
316 Kranz, 1983; Moore & Lockner, 1995), in which the cracks are oriented parallel to the di-
317 rection of the major principal stress (Wulff et al., 1999; Martin & Chandler, 1994; Moore

318 & Lockner, 1995). As the load applied to the specimen increases, a complex heterogeneous
 319 combination of tensile and shear stresses gets concentrated at the tips of the pre-existing
 320 flaws. Various experimental studies reveal that brittle fracture in compression is due to
 321 the development of the extensile microstresses. The macroscopic failure takes place due to
 322 the interaction of these tensile microcracks close to the tips of the pre-existing flaws. How-
 323 ever, tensile cracks are not solely responsible for the overall failure of the material (Lajtai,
 324 1974). Therefore, shear failure mechanism caused by the compressive stress concentration
 325 becomes active at later stages of the cracking process (Griffith, 1921; Lajtai, 1974). Once
 326 sufficient number of extensile cracks are formed, they start to interact, at this stage (crack
 327 damage stress threshold) the shear (frictional) cracking becomes dominant (Brace et al.,
 328 1966; Tapponnier & Brace, 1976; Martin & Chandler, 1994; Hajiabdolmajid et al., 2002;
 329 Jian-po et al., 2015). Martin and Chandler (1994) studied that the rock strength is made up
 330 of two components: friction and cohesion. The cohesive component is the primary strength
 331 component at early stages of loading and gets destroyed by the tensile cracking. Once suf-
 332 ficient damage has accumulated, the cohesion strength gets reduced and frictional strength
 333 component gets mobilized (Hajiabdolmajid et al., 2002). During this stage, high structural
 334 changes to the specimen takes place, with an increase in the density of microcracks by about
 335 sevenfold (Hallbauer et al., 1973).

336 The procedure adopted in this study for the quantification of the tensile and shear cracks
 337 accumulated in the rock specimen throughout the loading are described in the subsequent
 338 sections. The section deals with the cracking levels and the cracking mechanisms obtained
 339 through the experimental observations, it further illustrates the methodology used for the
 340 selection of the strain metrics evaluated from the 2D-DIC strain measurements to quantify
 341 the nonelastic damage into the rock specimen.

342 **3.1.1 Observation of Crack Initiation (CI) and Crack Damage (CD) using** 343 **AE Signatures**

344 As shown in Figure 2 (a & b), AE signatures were observed around the flaw tips in the
 345 specified region of interest, in sync with the 2D-DIC measurements. Several studies revealed
 346 that the AE hits acquired throughout the loading corresponds to the increasing number of
 347 microcracks and the energy of the signal denotes the magnitude of the cracking sources in
 348 materials (Lockner, 1993; Moradian et al., 2016). Therefore, to investigate the cracking
 349 levels, common parametric features of the AE waveform such as hits and energy emitted by
 350 the seismic sources were analyzed as a function of the normalized stress. The two important
 351 components in the brittle rock fracture that is crack initiation (CI) and crack damage (CD)
 352 thresholds were identified (Eberhardt et al., 1998).

353 Figure 2 (a & b) shows the rate and cumulative plots of the AE hits and AE energy as
 354 a function of applied stress normalized by the peak strength. The trend of the changes
 355 in the cumulative plots of AE hits due to increasing level of stress are consistent for all
 356 the specimen in the region of interest. Figure 2a shows that the initiation of significant
 357 AE activity in the cumulative hits plot occurred at 37-41% of the peak strength. This
 358 behavior has been detected in all the three rock specimen. Therefore, this point can be
 359 linked as the crack initiation point among the cracking levels. This cracking level detected
 360 by AE monitoring is consistent with the findings of several other studies corroborating it as
 361 the crack initiation (Pestman & Van Munster, 1996; Nicksiar & Martin, 2013). However,
 362 cumulative AE energy plot (Figure 2b) does not show any significant change in the trend
 363 at this stage (CI), which is consistent with the fact that microcracks have very low AE
 364 energy (Kim et al., 2015). When the load is further increased beyond crack initiation,
 365 it does not lead to the failure but the cracks become stable after propagating to some
 366 fraction of its initial length, known as the stable growth of the cracks. This can be seen by
 367 the constant increase in the cumulative hits plot. The cumulative AE energy plot is also
 368 constant and does not show any significant change in this region. This constant increase in
 369 the AE signal parameters indicate 'stable crack growth.' When the load reaches 85-90% of

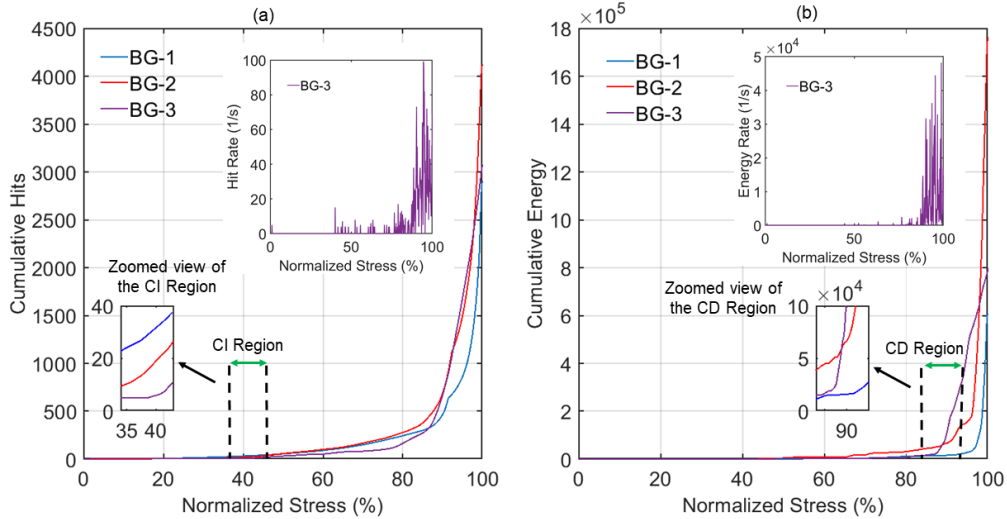


Figure 2. (a) Variation of cumulative AE hits as a function of normalized stress for the rock specimens BG-1,BG-2 and BG-3 at the specified ROI. The insets show the zoomed view of the CI region and the variation in the hit rate throughout loading for BG-3,(b) Variation of cumulative AE energy as a function of normalized stress for the rock specimen BG-1,BG-2 and BG-3 at the specified ROI. The insets show the zoomed view of the CD region and the variation of the energy rate throughout loading for BG-3.

370 the peak strength, the cumulative plots of AE hit and AE energy shows a sharp increase.
 371 This indicates the accumulation of microcracks to macrocracks, which is confirmed by the
 372 high amount of AE energy released at this stage. Therefore, the rise in the AE energy
 373 release can be called as 'macro-crack initiation'. Other researchers (Eberhardt et al., 1998;
 374 M. Diederichs, 2003; Nicksiar & Martin, 2012) have called this point as the 'crack damage'.
 375 At low levels of loading (0-30% of the failure stress), the AE parameters does not show
 376 any activity, whereas it has been found in previous studies that some AE signals can be
 377 seen in the initial loading stages due to crack closure and elastic deformation (Scholz, 1968;
 378 Eberhardt et al., 1998; Moradian et al., 2016). However, in these experiments, the analysis
 379 was mainly focused from the microcrack initiation to the failure of the sample, so the levels
 380 prior to the crack initiation was adopted to be quiet by setting a high threshold in the
 381 AE settings (~ 70 dB). Analysis of the digital images also did not reveal any significant
 382 information about the stages prior to crack initiation.

383 3.1.2 Observation of Crack Initiation (CI) and Crack Damage (CD) using 384 2D-DIC

385 The 2D-DIC technique was used to measure the strain along the specimen surface in the
 386 region of interest (ROI) and the damage was characterized based on the non-elastic strain
 387 measurements. The evolution of the non-elastic strain components in the rock specimen
 388 represents the initiation and growth of the microcracks. Therefore, in the present study, the
 389 inelastic components of the tensile and shear strain values were evaluated at various levels
 390 of loading for the analysis of the different mode of deformation.

391

3.1.3 Crack Initiation (CI) using Tensile Strain Measurements

392

393

394

395

396

397

398

399

400

401

402

403

404

405

406

407

408

409

410

As the damage progresses, strain accumulation takes place in the specimen. When the specimen is loaded under unconfined compression, major principal strain (ϵ_{11}) is caused along the longitudinal axis of the specimen, while the minor principal strain (ϵ_{22}) results due to the material expanding in the lateral direction (Poisson's effect). Based on the fact that the concentration of the local tensile stress at the tip of the flaw is the primary mode of deformation in brittle rocks (Moore & Lockner, 1995), the minor principal strain (ϵ_{22}) (extensile strain) distribution was studied in the specific region of interest for the three rock specimen to understand the effect of heterogeneity on the microcracking behavior. At low levels of loading (20% of the failure stress), the strain distribution showed a small standard deviation ($0.4 \text{ } \mu\epsilon$). As the stress level increases, the spread in the histogram and the standard deviation also increases. At 60% of the failure stress the standard deviation in strain distribution is around $1.1 \text{ } \mu\epsilon$ and goes upto $3 \text{ } \mu\epsilon$ at 95% of the failure stress. This indicates the increased heterogeneity in the strain field due to strain localization at higher levels of damage. As the stress level increases the histogram shift towards the left which shows the higher concentration of the extensile strains. The spread in the histogram also indicates the increase in the number of DIC grid points with higher magnitudes of the tensile strain. As shown in Figure 3 some of the DIC grid points show compressive strain in the tensile strain field which can be due to the heterogeneous distribution of strain at the pixel scale (M. S. Diederichs, 1999; Shirole et al., 2019).

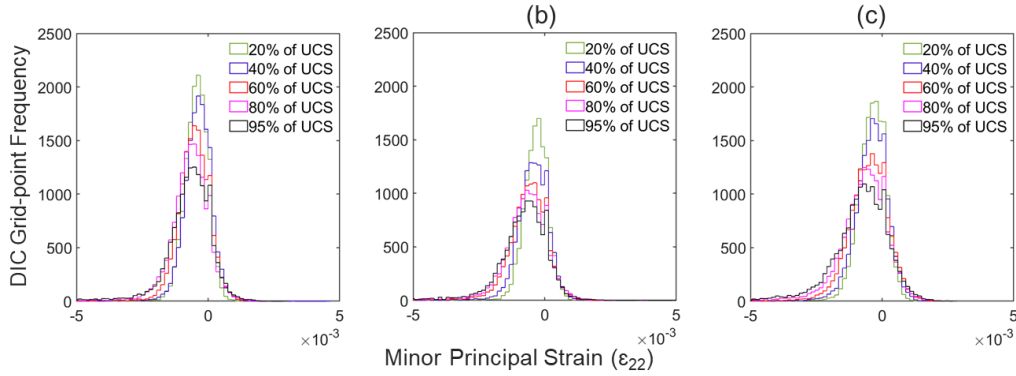


Figure 3. Histograms showing the minor principal strain distribution in the ROI for three prismatic Barre granite specimens: (a) BG-1,(b) BG-2,(c) BG-3. Negative (-) strains represent extension

411

412

413

In order to obtain the distribution of the localized tensile strain in the ROI, an apparent tensile strain (ϵ_{AT}^T), similar to the method adopted by (Song et al., 2013; Shirole et al., 2019), is used:

$$\epsilon_{AT}^T = \left| \sum_{i=1}^N \langle \epsilon_{22,i} \rangle \right| \quad (5)$$

414

415

416

417

418

where $\epsilon_{22,i}$ represents the minor principal strain at the i^{th} DIC grid point, and N is the total number of DIC grid points in the specified region of interest. For the computation of the apparent tensile strain, only negative strain values are taken into account. This apparent tensile strain contains both the elastic and inelastic component of the tensile strain present in the rock specimen.

419

420

As it is known that acoustic emission is released due to microcracking which leads to the irreversible increase in the rock volume, known as dilatancy. This increase in volume is

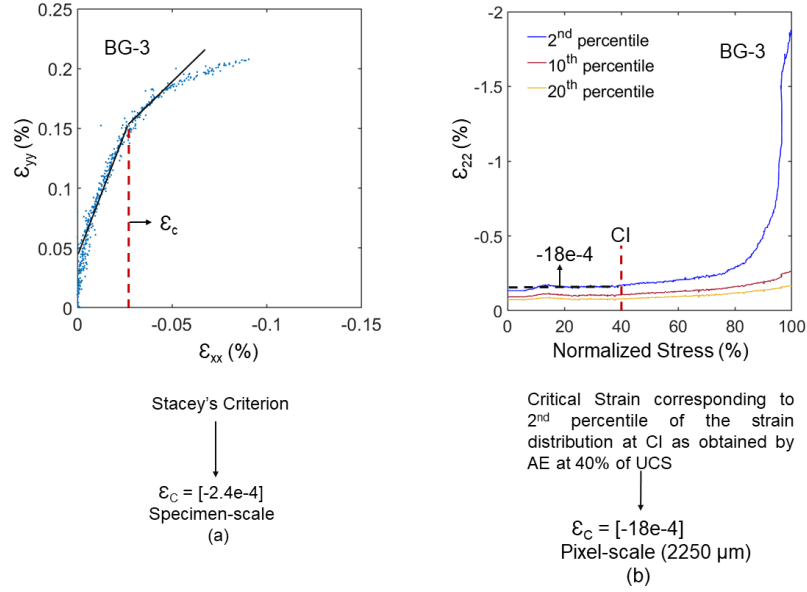


Figure 4. Procedure adopted for the evaluation of the critical threshold of tensile strain (ϵ_c) from DIC strain measurement (a) at specimen-scale (Stacey, 1981), (b) at pixel-scale (M. S. Diederichs, 1999; Shirole et al., 2019)

421 caused by the tensile opening. (Brace et al., 1966; Scholz, 1968; Sondergeld & Estey, 1982).
 422 Several experimental studies have shown that the initiation of the microcracking can be
 423 seen by a significant rise in the AE activity which is considered as the crack initiation
 424 stress (CI) (Eberhardt et al., 1999; Moradian et al., 2016) as shown in Figure 2. Similarly,
 425 the regions accumulated with the tensile microcracking are expected to be characterized
 426 by the tensile strain above some threshold limit at which the cracking initiates i.e. the
 427 plastic deformation takes place. With this in mind, and to establish the correlation between
 428 the microcracking observed through AE and DIC strain measurements, it is important to
 429 compute the nonelastic strain component which governs the plastic deformation in the rock
 430 specimen. To evaluate the nonelastic component, the critical tensile strain limit for Barre
 431 granite was estimated. The procedure adopted for the critical strain limit calculation is
 432 shown in Figure 4.

433 Due to the heterogeneous nature of rocks, the scale of strain measurement is also considered
 434 in order to calculate the critical threshold value of the tensile strain (ϵ_c). The heterogeneity
 435 in rocks create spatially uneven strain response to the applied stress, which causes irregular
 436 fluctuations in the strain distribution from the specimen scale to pixel scale. To accurately
 437 measure the critical limit of tensile strain the analysis was performed at both the specimen-
 438 scale and pixel-scale (Figure 4).

439 At the specimen-scale, Stacey(1981) strain criterion was used to evaluate the critical thresh-
 440 old value of the tensile strain. It has been established that the initiation of extensile micro-
 441 cracks in rocks is highlighted by the deviation in the slope of vertical strain (ϵ_{yy}) vs. lateral
 442 strain (ϵ_{xx}) plot from linear to non-linear. Figure 4a shows the plot of vertical strain vs.
 443 lateral strain for BG-3 in which the change in the slope can be observed corresponding to
 444 $-2.4e-4$ strain value. Therefore, the critical tensile strain limit (ϵ_c) at the specimen scale
 445 was estimated as $-2.4e-4$ (negative strain(-) represents extension). Since the DIC strain mea-
 446 surements are based on pixel-scale, the critical limit of tensile strain needs to be calculated
 447 at the pixel-scale. At the pixel-scale, the value of ϵ_c was calculated based on CI stress thresh-

448 old obtained through AE and was considered as 40% of the UCS. The 2nd, 10th and 20th
 449 percentiles of strain distribution were plotted as a function of the normalized stress (Figure
 450 4b) for BG-3. The second percentile of the strain distribution was chosen for the evaluation
 451 of CI threshold because of the following two reasons: (i) the strain distribution for second
 452 percentile followed a trend similar to the evolution of the acoustic emission (Eberhardt et
 453 al., 1998; Moradian et al., 2016; Shirole et al., 2019), and (ii) at CI stress level, very few
 454 tensile cracks were formed, which signifies that very few pixels have tensile strain value
 455 greater than the critical limit. As shown in Figure 4b, the pixel-scale value of the critical
 456 tensile strain limit was estimated as $-18e-4$. After the evaluation of the critical limit of the
 457 tensile strain (ϵ_c), the nonelastic apparent tensile strain (ϵ_{AT}^{NE}) was determined as follows:

$$\epsilon_{AT}^{NE} = \left| \sum_{i=1}^N \langle \epsilon_{22,i} \rangle \right|, \text{ where } \epsilon_{22,i} \leq \epsilon_c \quad (6)$$

458 The nonelastic apparent tensile strain component obtained through the above procedure was
 459 further utilized as a strain metrics to quantify the tensile deformations in the ROI region
 460 and to explicitly evaluate the extent of damage with the evolution of tensile cracks observed
 461 through the moment tensor analysis.

462 3.1.4 Crack Damage (CD) using Shear Strain Measurements

463 The nonelastic component of apparent shear strain was obtained using an approach similar
 464 to the quantification of the nonelastic apparent tensile strain component. As shear yield
 465 usually takes place along the plane of maximum shear strain (γ_{max}) (Jian-po et al., 2015;
 466 Shirole, Hedayat, & Walton, 2020), therefore maximum shear strain measurements were
 467 considered in this study for shear damage characterization. Figure 5 shows the maximum
 468 shear strain distribution at different levels of stress in the ROI. It is evident from the figure
 469 that as the stress on the rock specimen increases, the histogram shifts towards the right
 470 which indicates the increasing magnitude of the maximum shear strain. An increase in the
 471 heterogeneity of the maximum shear strain field can be observed at higher levels of stress
 472 which is consistent with the fact that shear cracking in rock dominates only beyond the
 473 crack damage (CD).

$$\gamma_{max} = \left| (\epsilon_{11} - \epsilon_{22}) / 2 \right| \quad (7)$$

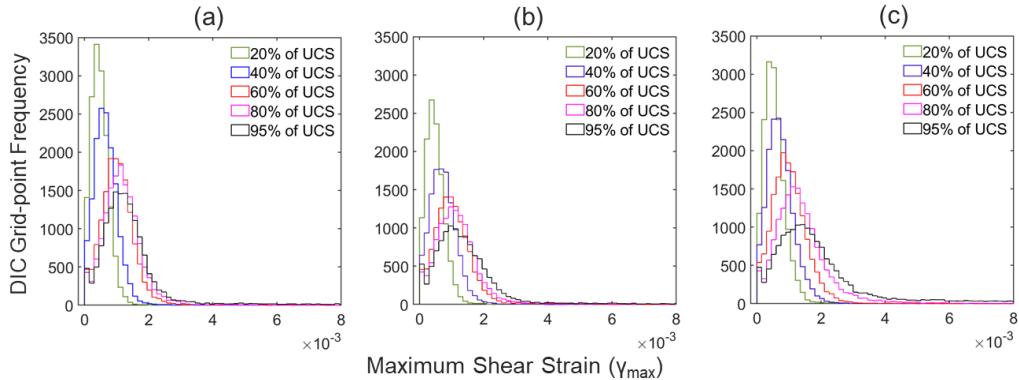


Figure 5. Histograms showing the maximum shear strain distribution in the ROI for three prismatic Barre granite specimens: (a) BG-1, (b) BG-2, (c) BG-3.

474 In this study, the damage due to tension has been characterized at pixel-scale measurements
 475 obtained through DIC. For the quantification of shear damage in the ROI, the non-elastic
 476 shear strain component needs to be evaluated at the pixel-scale. To estimate the pixel-scale
 477 non-elastic shear strain component, a critical threshold value of shear strain (γ_c) has been
 478 evaluated. As shear cracking in rocks primarily takes place beyond the CD stress level,
 479 therefore the rock specimen is expected to have less number of shear cracks as obtained
 480 through AE observations (Shirole, Hedayat, & Walton, 2020). Therefore, it is expected
 481 that at CD, very few pixels exhibit values of γ_{max} greater than γ_c . This shows that the
 482 critical shear strain limit (γ_c) should correspond to a small maximum shear strain (γ_{max})
 483 distribution percentile. Figure 6 explains the procedure adopted for the determination of
 484 γ_c . The appropriate percentile distribution was chosen based on the fact that since shear
 485 cracking in rocks accelerates beyond CD stress level, the γ_{max} percentile corresponding to
 486 γ_c should show a deviation from linearity beyond CD threshold. To determine the value
 487 of γ_c , several percentiles of γ_{max} were plotted as a function of normalized stress (Figure
 488 6). The strain distribution in the ROI follows a linear trend upto a certain stress level and
 489 then deviates at higher magnitudes of stress ($\sim 80\%$ of the failure stress and above) which
 490 is consistent with the AE observations as shown in figure (2) for the rock specimen BG-3.
 491 Figure 6 shows that the data deviates from the linear trend at $\sim 80\%$ of the UCS and above.
 492 This deviation from linearity can be associated with the unstable growth of the microcracks
 493 (Moradian et al., 2016). The 5th percentile of the γ_{max} strain variation does not show any
 494 significant change in the slope, but the 0.5th percentile and 0.1st percentile showed a distinct
 495 deviation from linearity at around 80% of the failure stress. The 0.5th percentile strain-field
 496 was chosen for the evaluation of (γ_c) because of two reasons (i) it followed a trend similar
 497 to the AE observations, (ii) it is consistent with the findings of the numerical model for
 498 granitic rocks proposed by (Sinha et al., 2020) which states that 0.3% -0.5% of grains in the
 499 micro-mechanical model showed shear damage at CD.

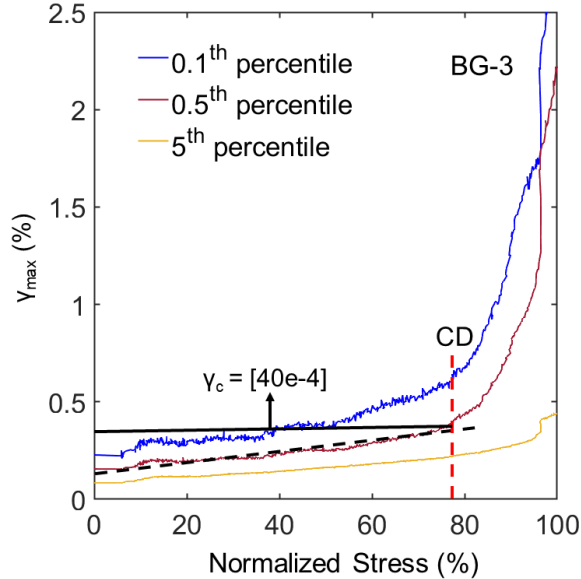


Figure 6. Procedure followed to obtain the pixel-scale critical shear strain limit (γ_c). The critical limit for maximum shear strain was obtained as ($40e-4$) corresponding to the 0.5th percentile of the maximum shear strain variation (Shirole, Hedayat, & Walton, 2020)

500 The critical limit of the maximum shear strain (γ_c) obtained through the above procedure
 501 was (40e-4), which is greater than the critical limit of the tensile strain ($\epsilon_c = -18e - 5$)
 502 and also consistent with the previous observations that damage in brittle rocks initiate in
 503 tension prior to shear (M. Diederichs et al., 2004). These observations are also consistent
 504 with the CWFS (cohesion weakening and frictional strengthening) model proposed by Ha-
 505 jjabdolmajid et al. (2002). After the determination of the specific γ_c , procedure similar to
 506 the quantification of tensile damage was adopted to evaluate the total apparent shear strain
 507 and the non-elastic component of shear strain as shown in equation 8 and 9. The strain
 508 described in the above sections are considered as the apparent one, because in some cases
 509 it does not hold true due to the evolution of damage (Song et al., 2013)

$$\gamma_{AS}^T = \left| \sum_{i=1}^N \gamma_{max,i} \right| \quad (8)$$

$$\gamma_{AS}^{NE} = \left| \sum_{i=1}^N \langle \gamma_{max,i} \rangle \right|, \text{ where } \gamma_{max,i} \geq \gamma_c \quad (9)$$

510 In equation 8 and 9, γ_{max} represents the maximum shear strain across the ROI at the N
 511 number of DIC grid points which in this case is 15770. Therefore, the apparent maximum
 512 shear strain can be defined as the summation of the maximum shear strain across the
 513 specified region of interest. The non-elastic component is evaluated by considering the
 514 maximum shear strain greater than the estimated critical value at the DIC grid points.

515 3.2 Crack Source Mechanisms

516 As discussed in the previous section that the progression of tensile and shear damage in
 517 rocks can be better understood on the basis of the non-elastic component of tensile and shear
 518 strain measurements. Therefore this section deals with the spatiotemporal distribution of
 519 the different crack source mechanism obtained through the 2D-DIC and AE techniques and
 520 their correlation.

521 Scholz (1968) (Scholz, 1968) reported that AE signals recorded during a rock fracture ex-
 522 periment, shows a rate of occurrence that can be correlated with the nonelastic stress-strain
 523 behavior of the rock. He conducted experiments on Westerly granite under unconfined com-
 524 pression and correlated the inelastic volumetric strain with the rate of AE, however the
 525 mechanism of cracking was not discussed in the study. A similar technique has been applied
 526 in this study where the occurrence of AE events were correlated with the DIC strain mea-
 527 surements with a major emphasis on the cracking mechanism. In particular, the evolution of
 528 different crack types obtained through moment tensor analysis were observed with increas-
 529 ing levels of nonelastic strain components (tensile and shear). Understanding this behavior
 530 is important to observe the extent of shear and tensile deformation in the rock specimen
 531 throughout the damage. With this in mind, the evolution of tensile and shear cracks and
 532 the calculated non-elastic component of tensile and shear strain has been plotted as a func-
 533 tion of loading in the ROI for each rock specimen (Figure 7). The detailed description is
 534 provided in the following subsections.

535 3.2.1 Temporal Evolution of Crack Mechanisms

536 Figure 7a shows a consistent relationship between the evolution of the tensile cracks detected
 537 by AE and the non-elastic component of tensile strain detected by DIC, throughout the
 538 loading for all the three rock specimen. In uniaxial compression test, the CI threshold
 539 denotes the initiation of microcracks (also obtained from AE) in the form of stable extensile
 540 microcracks governed by the non-elastic tensile deformation in rocks (Lockner, 1993). This
 541 is quite evident from Figure 7a which shows a rise in the evolution of the tensile cracks in

542 the CI region. The nonelastic tensile strain component which is a metric of damage around
 543 the flaw tips, also shows a significant rise around 30-40% of UCS. However, the rise in the
 544 AE crack mechanism occurred earlier than the strain values, this can be due to the fact that
 545 the DIC is related only to the surface strain measurements, whereas AE accounts for the
 deformation in the rock volume.

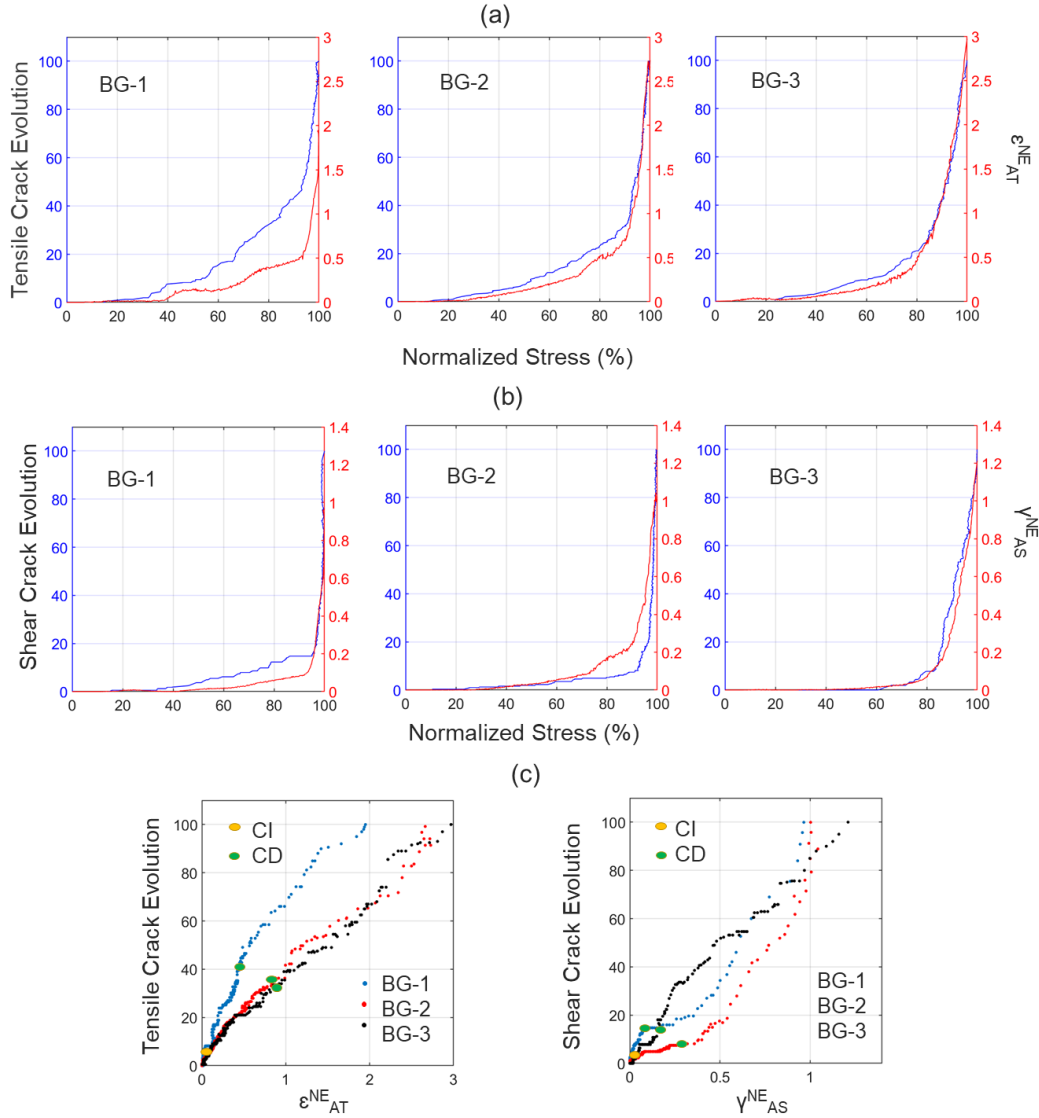


Figure 7. (a) Variation of tensile crack evolution (AE) and Non-elastic component of tensile strain (DIC) in the ROI for three Barre granite specimens, (b) Variation of shear crack evolution (AE) and Non-elastic component of maximum shear strain (DIC) in the ROI for three Barre granite specimens, (c) Correlation between the type of crack and nonelastic strain component in the ROI for the three rock specimens, the CI and CD has been distinguished by the yellow and green circles on the map.

546

547 When the load is increased further (from CI to CD), the nonelastic tensile strain increases
 548 with the increasing number of tensile cracks. The curve shows an accelerated increase in the
 549 nonelastic tensile strain around the CD region (80%-90% of UCS) which is consistent with

550 the fact that the damage in brittle rocks primarily occur due to the local tensile stresses
 551 even if the rocks are subjected to compressive stress field. From these observations, it can
 552 be concluded that the nonelastic component of the tensile strain is a good representative
 553 of the tensile crack evolution in the rock specimen and it can be used to quantify the
 554 initiation, growth and coalescence of the extensile microcracking in rocks. Figure 7c shows
 555 the correlation between the cumulative number of tensile cracks and non-elastic tensile strain
 556 component evaluated through DIC full-field strain measurements in the ROI. In particular,
 557 a near linear correlation can be seen between the tensile crack and non-elastic tensile strain
 558 field. At higher levels of stress the trend becomes non-linear because of the loss in correlation
 559 of strain measurements. This observation is consistent with the findings of many direct
 560 microscopic observational approaches (e.g. optical microscope, scanning electron microscopy
 561 (SEM) etc.) which indicate that crack initiation takes place in tensile mode at the flaw tips
 562 at early stages of loading in the rock specimen.

563 Since the nonelastic apparent maximum shear strain (γ_{AS}^{NE}) can be used as a metric for the
 564 characterization of shear damage in rocks, the evolution of shear cracks and the nonelastic
 565 component of maximum shear strain was plotted as a function of normalized stress for the
 566 three rock specimen in the ROI (Figure 7b). The curves show a sharp increase around
 567 the CD threshold (80% – 90%) and above. These observations are consistent with many
 568 experimental and numerical evaluation which states that the microcracks induced by the
 569 tensile strain begin to coalesce beyond the CD stress threshold and causes the shear-strain
 570 induced microcracks to dominate (M. Diederichs, 2003; M. Diederichs et al., 2004; J. Peng
 571 et al., 2017). These results also indicate that shear strain at the pixel scale represents a
 572 more local level of shear damage and thus can be correlated with the AE crack mechanism.
 573 A similar observation can be seen in figure 7c, which shows the ratio of the shear cracks
 574 with respect to total number of shear cracks at each stress level as a function of nonelastic
 575 maximum shear strain. The trend shows a near linear correlation, although the number of
 576 shear cracks between the CI and CD limit is very low. After the CD, an increase in the
 577 number of shear cracks can be seen.

578 The results in the present study shows that with the evolution of shear cracks, the nonelastic
 579 component of shear strain increases by seven to ninefolds from the CD limit to the failure
 580 of the specimen. These observations are consistent with the conclusions of several other
 581 studies such as Martin and Chandler (1994), Diederichs et al.(2003), Martin et al. (2010),
 582 Sinha and Walton (2020) and the CWFS (cohesion weakening and frictional strengthening)
 583 model proposed by Hajiabdolmajid et al. (2002).

584 The consistent correlation between the temporal evolution of tensile and shear cracks with
 585 the nonelastic DIC strain components provides a better understanding about the mechanism
 586 of microfracture accumulation and failure in brittle rocks. The results suggest that the
 587 formation of macrocrack involves the existence of both tensile and shear microcracks but
 588 the proportion of their evolution is different as the damage progresses. As shown in figure
 589 7a the evolution of tensile microcracks and nonelastic tensile strain shows an increasing
 590 trend between the CI and CD which can be associated with the tensile opening at the
 591 macroscale. Once the tensile cracking has occurred at the macroscale, the ratio of shear crack
 592 and nonelastic shear strain dominates (beyond CD) this could be due to the separation
 593 caused by the tensile opening in the rock specimen. Thus, the increasing trend in the
 594 evolution of shear cracks (from CD to the failure of the rock specimen) can be interpreted as
 595 the shear macrocrack formation. Although few shear microcracks can be observed between
 596 the CI and CD (figure 7b) this can be interpreted as the widening of the fracture process
 597 zone (L. N. Y. Wong & Xiong, 2018). In addition to this, the present experimental results
 598 also confirms explicitly an interesting finding that the strain metrics applied in the present
 599 study can be used as an effective tool to identify the various cracking levels in rock damage
 600 in combination with the AE monitoring.

3.2.2 Spatial Distribution of Crack Mechanisms

601

602 The evolution of the mode of fracture through AE was obtained using the moment tensor
 603 inversion technique. In order to analyze the mode of deformation from DIC strain measure-
 604 ments, the normal and shear component of strain were calculated by adopting a procedure
 605 similar to the method proposed by Tal et al. (2016). To analyze the strain in the ROI,
 606 the principal strain component was calculated for all the grid points in the specific region
 607 (ROI). In order to get the damage features (microcracks), only those grid points in the ROI
 608 were selected in which the difference between the principal strain component was larger
 609 than 0.01 (1%) (Tal et al., 2016) and where more than 5 grid points remained (filter size
 610 is 5, strain resolution of DIC was $2250\mu\epsilon$). This filtering of the strain map was done to
 611 eliminate the noise with a conservative approach so as to ensure that the damage features
 612 obtained through the image based strain profiles after filtering had minimum measurement
 613 errors. These damage features were considered as the microcracks and their orientation was
 614 obtained through visual inspection. Once the orientation was identified, the normal and
 615 shear components of the strains were calculated by resolving the values perpendicular and
 616 parallel to the crack trend. Observations from the two techniques, that is the evolution of
 617 the tensile and shear cracks through moment tensors of AE and the mode of deformation
 618 obtained through image based strain profiles from DIC were plotted at different levels of
 619 stress. Figures 8 and 9 shows the spatial distribution of the AE cracks obtained through
 620 the moment tensor analysis and the normal and shear component of the strain obtained
 621 through DIC in the ROI for BG-3. The evolution of tensile crack is compared with the
 622 normal component of strain (Figure 8) and the shear crack evolution is compared with the
 623 shear component of strain along the crack trend (Figure 9).

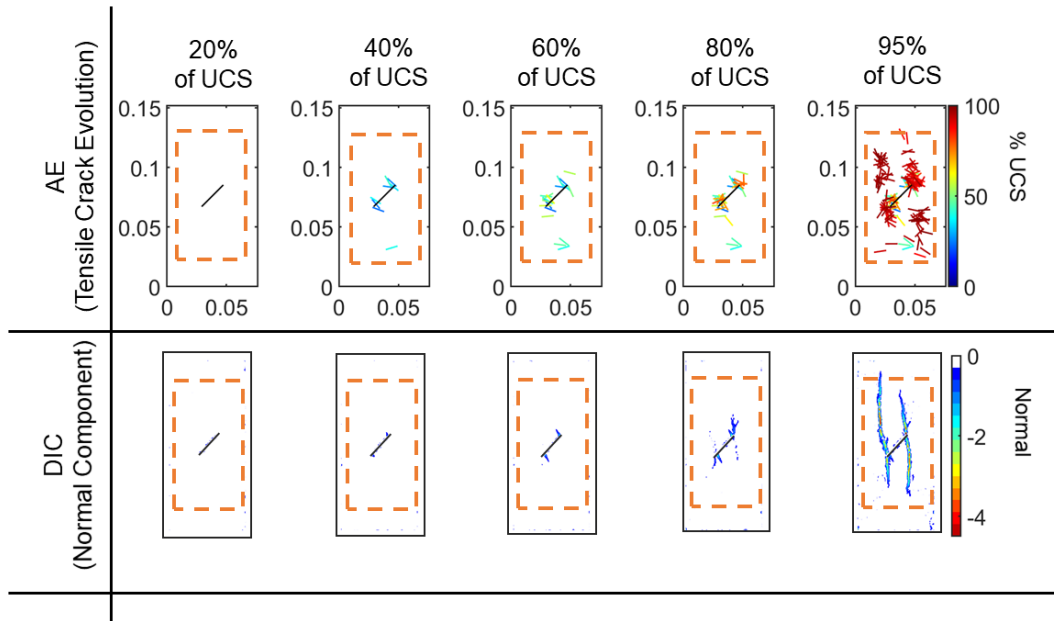


Figure 8. Comparison between the mode of deformation obtained through AE (tensile cracks) and DIC (normal component of strain) at different levels of stress in the ROI for BG-3.

624

625 Figure 8 shows that the tensile cracks initiated close to the flaw tips at around 40% of UCS
 626 which is the CI for BG-3. At the same stress level, the normal mode of deformation can also
 627 be seen in the strain maps. Few microcracks through AE can be seen in the lower region of
 628 the specimen which is not evident in the DIC strain maps, this could be due to the damage
 along the depth of the specimen which cannot be observed in the image analysis. Moreover,

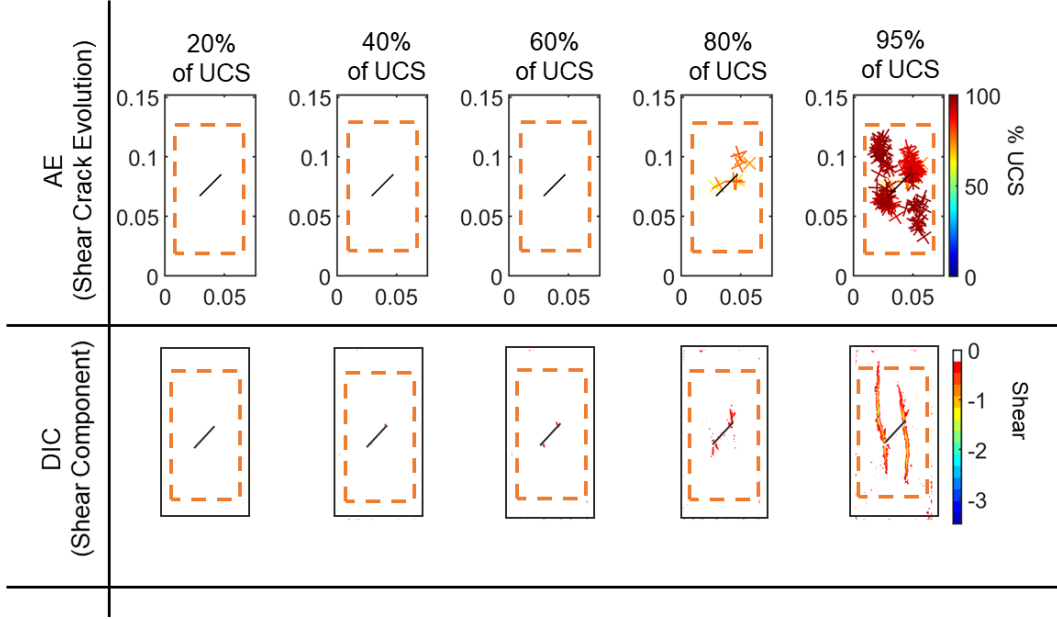


Figure 9. Comparison between the mode of deformation obtained through AE (shear cracks) and DIC (shear component of strain) at different levels of stress in the ROI for BG-3

629 as the loading increases, the microcracks propagate subparallel along the direction of the
 630 major principal stress. As expected, the strain concentration at the flaw tips increases with
 631 increasing levels of stress.

632 Figure 9 shows the evolution of the shear cracks from the AE moment tensor analysis and
 633 the shear component of strain resolved parallel to the crack trend at different levels of stress
 634 for BG-3. At initial stages (40-50% of the failure stress) no shear cracking can be seen
 635 through both the techniques. The shear cracks initiated at higher levels of stress (60-80% of
 636 the failure stress), which is very close to the CD stress threshold of the rock specimen. The
 637 evolution of shear microcracks between the CI and CD is associated with the widening of the
 638 fracture process zone. Similarly, some shear strain concentration can be seen at 60% of
 639 the failure stress which can be due to the evolution of few shear microcracks in between CI
 640 to CD. The results of the shear component of strain measurements are very consistent with
 641 the shear crack evolution at later stages of loading. Near failure (95% of UCS) both modes
 642 of deformation (tensile and shear) was observed, but the shear mode is more dominant.

643 These observations experimentally illustrate the relationship between the mode of deforma-
 644 tion obtained through image based strain profiles and the process of microfracturing
 645 obtained through the moment tensors of AE. The results are consistent with the previous
 646 observations (Tapponnier & Brace, 1976; Paterson & Wong, 2005) that showed that micro-
 647 cracks initiate in tension in low porosity brittle rocks further extending to shear damage.
 648 Although it has been previously observed that the nonelastic strain component shows a con-
 649 sistent relationship with the tensile and shear damage in rocks, these results further confirms
 650 that the overall deformation in rocks subjected to various levels of stress is a combination
 651 of both (normal and shear) modes of deformation.

652 4 Conclusions

653 In this study, the temporal-spatial evolution of stress-induced microcracks and the pro-
 654 portion of different modes of cracking around the flaw tip was studied for Barre granite

specimen with an existing flaw under unconfined compression. The moment tensor analysis was employed on the AE waveforms for the evaluation of the crack mechanism in rocks subjected to unconfined compression and the non-elastic tensile and shear strain component was computed from the 2D-DIC strain measurements. Based on the results from the previous studies that AE represents the inelastic deformation (microcracking) in the rocks, the damage mechanism obtained through AE was linked with the non-elastic tensile and shear strain field evaluated from the DIC strain monitoring.

The 2D-DIC strain maps showed that as the load increases the heterogeneity in the strain field increases due to the accumulated damage in the rock microstructure. Based on the fact that the damage process in rocks initiate in tension, the tensile strain distribution was analyzed in the ROI. Similarly, to analyze the evolution of shear cracks, the distribution of shear strain was observed through the maximum apparent shear strain in the ROI. In particular, the nonelastic tensile strain (ϵ_{AT}^{NE}) and the nonelastic shear strain (γ_{AS}^{NE}) distribution was analyzed in the specific region of interest. To obtain the non-elastic component of strains, the critical limit for tensile (ϵ_c) and shear strain (γ_c) were computed above which the strain was considered as non-elastic. The results showed that the evolution of tensile cracks obtained through the moment tensor analysis and the non-elastic apparent tensile strain followed a consistent trend throughout the loading for all the experiments. Similar observation was seen for the evolution of shear cracks and non-elastic shear strain.

To analyze the mode of deformation from the DIC based strain profiles, the normal and shear components of strain along the damage features were computed. Using filtering techniques to the 2D-DIC strain data, linear damage features (microcracks) and their orientation were obtained from the image based strain profiles. Once the linear features and their orientation was identified, the strain field was resolved into the normal and shear components along the crack length. The study showed a consistent trend between the AE and DIC observations in the ROI for the shear and normal deformations. In particular, tensile deformation was observed throughout the loading initiating from the CI stress threshold while shear deformation dominated closer to the peak stress.

ACKNOWLEDGMENTS

This research is supported by the U.S. Department of Energy, Office of Basic Energy Sciences, under Award Number DE-SC0019117. Interested readers can obtain the data related to this research article from <https://figshare.com/s/56776f9041c56a3f29bc>.

References

- Bazant, Z. P., & Kazemi, M. (1990). Determination of fracture energy, process zone length and brittleness number from size effect, with application to rock and concrete. *International Journal of fracture*, *44*(2), 111–131.
- Bieniawski, Z. (1967). Mechanism of brittle fracture of rock: part ii—experimental studies. In *International journal of rock mechanics and mining sciences & geomechanics abstracts* (Vol. 4, pp. 407–423).
- Bieniawski, Z. T. (1967). Mechanism of brittle fracture of rock: part i—theory of the fracture process. In *International journal of rock mechanics and mining sciences & geomechanics abstracts* (Vol. 4, pp. 395–406).
- Bourcier, M., Bornert, M., Dimanov, A., Héripré, E., & Raphanel, J. (2013). Multiscale experimental investigation of crystal plasticity and grain boundary sliding in synthetic halite using digital image correlation. *Journal of Geophysical Research: solid earth*, *118*(2), 511–526.
- Brace, W., Paulding Jr, B., & Scholz, C. (1966). Dilatancy in the fracture of crystalline rocks. *Journal of Geophysical Research*, *71*(16), 3939–3953.
- Bruck, H., McNeill, S., Sutton, M. A., & Peters, W. (1989). Digital image correlation using newton-raphson method of partial differential correction. *Experimental mechanics*,

- 705 29(3), 261–267.
- 706 Chang, S.-H., & Lee, C.-I. (2004). Estimation of cracking and damage mechanisms in rock
707 under triaxial compression by moment tensor analysis of acoustic emission. *International*
708 *Journal of Rock Mechanics and Mining Sciences*, 41(7), 1069–1086.
- 709 Cheng, J.-L., Yang, S.-Q., Chen, K., Ma, D., Li, F.-Y., & Wang, L.-M. (2017). Uniaxial
710 experimental study of the acoustic emission and deformation behavior of composite
711 rock based on 3d digital image correlation (dic). *Acta Mechanica Sinica*, 33(6), 999–
712 1021.
- 713 Cheng, Y., & Wong, L. N. Y. (2018). Microscopic characterization of tensile and shear
714 fracturing in progressive failure in marble. *Journal of Geophysical Research: Solid*
715 *Earth*, 123(1), 204–225.
- 716 Crider, J. G. (2015). The initiation of brittle faults in crystalline rock. *Journal of Structural*
717 *Geology*, 77, 159–174.
- 718 Dai, F., & Xia, K. (2010). Loading rate dependence of tensile strength anisotropy of barre
719 granite. *Pure and applied geophysics*, 167(11), 1419–1432.
- 720 Diederichs, M. (2003). Manuel rocha medal recipient rock fracture and collapse under low
721 confinement conditions. *Rock Mechanics and Rock Engineering*, 36(5), 339–381.
- 722 Diederichs, M., Kaiser, P., & Eberhardt, E. (2004). Damage initiation and propagation in
723 hard rock during tunnelling and the influence of near-face stress rotation. *International*
724 *Journal of Rock Mechanics and Mining Sciences*, 41(5), 785–812.
- 725 Diederichs, M. S. (1999). *Instability of hard rockmasses, the role of tensile damage and*
726 *relaxation* (Unpublished doctoral dissertation). University of Waterloo.
- 727 Dong, W., Wu, Z., Zhou, X., Wang, N., & Kastiukas, G. (2017). An experimental study on
728 crack propagation at rock-concrete interface using digital image correlation technique.
729 *Engineering fracture mechanics*, 171, 50–63.
- 730 Eberhardt, E., Stead, D., Stimpson, B., & Read, R. (1998). Identifying crack initiation and
731 propagation thresholds in brittle rock. *Canadian geotechnical journal*, 35(2), 222–233.
- 732 Eberhardt, E., Stimpson, B., & Stead, D. (1999). Effects of grain size on the initiation and
733 propagation thresholds of stress-induced brittle fractures. *Rock mechanics and rock*
734 *engineering*, 32(2), 81–99.
- 735 Fortin, J., Stanchits, S., Dresen, G., & Gueguen, Y. (2009). Acoustic emissions monitor-
736 ing during inelastic deformation of porous sandstone: comparison of three modes of
737 deformation. *Pure and Applied Geophysics*, 166(5-7), 823–841.
- 738 Fredrich, J. T., Evans, B., & Wong, T.-F. (1989). Micromechanics of the brittle to plastic
739 transition in carrara marble. *Journal of Geophysical Research: Solid Earth*, 94(B4),
740 4129–4145.
- 741 Ghamgosar, M., Erarslan, N., & Williams, D. (2017). Experimental investigation of fracture
742 process zone in rocks damaged under cyclic loadings. *Experimental Mechanics*, 57(1),
743 97–113.
- 744 Goldsmith, W., Sackman, J., & Ewerts, C. (1976). Static and dynamic fracture strength
745 of barre granite. In *International journal of rock mechanics and mining sciences &*
746 *geomechanics abstracts* (Vol. 13, pp. 303–309).
- 747 Graham, C. C., Stanchits, S., Main, I. G., & Dresen, G. (2010). Comparison of polarity
748 and moment tensor inversion methods for source analysis of acoustic emission data.
749 *International journal of rock mechanics and mining sciences (Oxford, England: 1997)*,
750 47(1), 161.
- 751 Griffith, A. A. (1921). Vi. the phenomena of rupture and flow in solids. *Philosophical trans-*
752 *actions of the royal society of london. Series A, containing papers of a mathematical*
753 *or physical character*, 221(582-593), 163–198.
- 754 Guo, M., Alam, S. Y., Bendimerad, A. Z., Grondin, F., Rozière, E., & Loukili, A. (2017).
755 Fracture process zone characteristics and identification of the micro-fracture phases in
756 recycled concrete. *Engineering Fracture Mechanics*, 181, 101–115.
- 757 Hajiabdolmajid, V., Kaiser, P. K., & Martin, C. (2002). Modelling brittle failure of rock.
758 *International Journal of Rock Mechanics and Mining Sciences*, 39(6), 731–741.
- 759 Hallbauer, D., Wagner, H., & Cook, N. (1973). Some observations concerning the micro-

- 760 scopic and mechanical behaviour of quartzite specimens in stiff, triaxial compression
761 tests. In *International journal of rock mechanics and mining sciences & geomechanics*
762 *abstracts* (Vol. 10, pp. 713–726).
- 763 Hampton, J., Gutierrez, M., Matzar, L., Hu, D., & Frash, L. (2018). Acoustic emission char-
764 acterization of microcracking in laboratory-scale hydraulic fracturing tests. *Journal*
765 *of Rock Mechanics and Geotechnical Engineering*, *10*(5), 805–817.
- 766 Hedayat, A., Pyrak-Nolte, L. J., & Bobet, A. (2014). Detection and quantification of slip
767 along non-uniform frictional discontinuities using digital image correlation. *Geotech-*
768 *nical Testing Journal*, *37*(5), 786–799.
- 769 Hedayat, A., & Walton, G. (2017). Laboratory determination of rock fracture shear stiffness
770 using seismic wave propagation and digital image correlation. *Geotechnical Testing*
771 *Journal*, *40*(1), 92–106.
- 772 Iqbal, M., & Mohanty, B. (2007). Experimental calibration of isrm suggested fracture
773 toughness measurement techniques in selected brittle rocks. *Rock Mechanics and Rock*
774 *Engineering*, *40*(5), 453.
- 775 Jian-po, L., Yuan-hui, L., Shi-da, X., Shuai, X., & Chang-yu, J. (2015). Cracking mecha-
776 nisms in granite rocks subjected to uniaxial compression by moment tensor analysis
777 of acoustic emission. *Theoretical and Applied Fracture Mechanics*, *75*, 151–159.
- 778 Kao, C.-S., Tarokh, A., Biolzi, L., & Labuz, J. F. (2016). Inelastic strain and damage in
779 surface instability tests. *Rock Mechanics and Rock Engineering*, *49*(2), 401–415.
- 780 Kim, J.-S., Lee, K.-S., Cho, W.-J., Choi, H.-J., & Cho, G.-C. (2015). A comparative
781 evaluation of stress–strain and acoustic emission methods for quantitative damage
782 assessments of brittle rock. *Rock Mechanics and Rock Engineering*, *48*(2), 495–508.
- 783 Kranz, R. L. (1979). Crack growth and development during creep of barre granite. In
784 *International journal of rock mechanics and mining sciences & geomechanics abstracts*
785 (Vol. 16, pp. 23–35).
- 786 Kranz, R. L. (1983). Microcracks in rocks: a review. *Tectonophysics*, *100*(1-3), 449–480.
- 787 Kurz, J. H., Grosse, C. U., & Reinhardt, H.-W. (2005). Strategies for reliable automatic
788 onset time picking of acoustic emissions and of ultrasound signals in concrete. *Ultra-*
789 *sonics*, *43*(7), 538–546.
- 790 Lajtai, E. (1974). Brittle fracture in compression. *International Journal of Fracture*, *10*(4),
791 525–536.
- 792 Li, B. Q., da Silva, B. G., & Einstein, H. (2019). Laboratory hydraulic fracturing of granite:
793 acoustic emission observations and interpretation. *Engineering Fracture Mechanics*,
794 *209*, 200–220.
- 795 Li, B. Q., & Einstein, H. H. (2017). Comparison of visual and acoustic emission observa-
796 tions in a four point bending experiment on barre granite. *Rock Mechanics and Rock*
797 *Engineering*, *50*(9), 2277–2296.
- 798 Lin, Q., & Labuz, J. F. (2013). Fracture of sandstone characterized by digital image
799 correlation. *International Journal of Rock Mechanics and Mining Sciences*, *60*, 235–
800 245.
- 801 Lin, Q., Wan, B., Wang, Y., Lu, Y., & Labuz, J. F. (2019). Unifying acoustic emission and
802 digital imaging observations of quasi-brittle fracture. *Theoretical and Applied Fracture*
803 *Mechanics*, *103*, 102301.
- 804 Lin, Q., Yuan, H., Biolzi, L., & Labuz, J. F. (2014). Opening and mixed mode fracture pro-
805 cesses in a quasi-brittle material via digital imaging. *Engineering Fracture Mechanics*,
806 *131*, 176–193.
- 807 Lockner, D. (1993). The role of acoustic emission in the study of rock fracture. In *In-*
808 *ternational journal of rock mechanics and mining sciences & geomechanics abstracts*
809 (Vol. 30, pp. 883–899).
- 810 Maeda, N. (1985). A method for reading and checking phase times in autoprocessing system
811 of seismic wave data. *Zisin*, *38*, 365–379.
- 812 Martin, C., & Chandler, N. (1994). The progressive fracture of lac du bonnet granite. In
813 *International journal of rock mechanics and mining sciences & geomechanics abstracts*
814 (Vol. 31, pp. 643–659).

- 815 McClintock, F. A., & Irwin, G. (1965). Plasticity aspects of fracture mechanics. In *Fracture*
816 *toughness testing and its applications*. ASTM International.
- 817 Modiriasari, A., Bobet, A., & Pyrak-Nolte, L. J. (2017). Active seismic monitoring of
818 crack initiation, propagation, and coalescence in rock. *Rock Mechanics and Rock*
819 *Engineering*, *50*(9), 2311–2325.
- 820 Moore, D. E., & Lockner, D. (1995). The role of microcracking in shear-fracture propagation
821 in granite. *Journal of Structural Geology*, *17*(1), 95–114.
- 822 Moradian, Z., Einstein, H. H., & Ballivy, G. (2016). Detection of cracking levels in brittle
823 rocks by parametric analysis of the acoustic emission signals. *Rock Mechanics and*
824 *Rock Engineering*, *49*(3), 785–800.
- 825 Morgan, S. P., Johnson, C. A., & Einstein, H. H. (2013). Cracking processes in barre gran-
826 ite: fracture process zones and crack coalescence. *International Journal of Fracture*,
827 *180*(2), 177–204.
- 828 Nasserri, M., Grasselli, G., & Mohanty, B. (2010). Fracture toughness and fracture roughness
829 in anisotropic granitic rocks. *Rock Mechanics and Rock Engineering*, *43*(4), 403–415.
- 830 Nicksiar, M., & Martin, C. (2012). Evaluation of methods for determining crack initiation
831 in compression tests on low-porosity rocks. *Rock Mechanics and Rock Engineering*,
832 *45*(4), 607–617.
- 833 Nicksiar, M., & Martin, C. (2013). Crack initiation stress in low porosity crystalline and
834 sedimentary rocks. *Engineering Geology*, *154*, 64–76.
- 835 Ohtsu, M. (1991). Simplified moment tensor analysis and unified decomposition of acoustic
836 emission source: application to in situ hydrofracturing test. *Journal of Geophysical*
837 *Research: Solid Earth*, *96*(B4), 6211–6221.
- 838 Ohtsu, M. (1995). Acoustic emission theory for moment tensor analysis. *Research in*
839 *Nondestructive Evaluation*, *6*(3), 169–184.
- 840 Pan, B., Qian, K., Xie, H., & Asundi, A. (2009). Two-dimensional digital image correlation
841 for in-plane displacement and strain measurement: a review. *Measurement science*
842 *and technology*, *20*(6), 062001.
- 843 Paterson, M. S., & Wong, T.-f. (2005). *Experimental rock deformation-the brittle field*.
844 Springer Science & Business Media.
- 845 Peng, J., Wong, L. N. Y., & Teh, C. I. (2017). Influence of grain size heterogeneity
846 on strength and microcracking behavior of crystalline rocks. *Journal of Geophysical*
847 *Research: Solid Earth*, *122*(2), 1054–1073.
- 848 Peng, S., & Johnson, A. (1972). Crack growth and faulting in cylindrical specimens of
849 chelmsford granite. In *International journal of rock mechanics and mining sciences &*
850 *geomechanics abstracts* (Vol. 9, pp. 37–86).
- 851 Peng, S. S. (1975). A note on the fracture propagation and time-dependent behavior of rocks
852 in uniaxial tension. In *International journal of rock mechanics and mining sciences &*
853 *geomechanics abstracts* (Vol. 12, pp. 125–127).
- 854 Pestman, B., & Van Munster, J. (1996). An acoustic emission study of damage development
855 and stress-memory effects in sandstone. In *International journal of rock mechanics and*
856 *mining sciences & geomechanics abstracts* (Vol. 33, pp. 585–593).
- 857 Reches, Z., & Lockner, D. A. (1994). Nucleation and growth of faults in brittle rocks.
858 *Journal of Geophysical Research: Solid Earth*, *99*(B9), 18159–18173.
- 859 Richards, P. G., & Aki, K. (1980). *Quantitative seismology: Theory and methods*. Freeman.
- 860 Scholz, C. (1968). Microfracturing and the inelastic deformation of rock in compression.
861 *Journal of Geophysical Research*, *73*(4), 1417–1432.
- 862 Schwartz, E., Saralaya, R., Cuadra, J., Hazeli, K., Vanniamparambil, P. A., Carmi, R.,
863 ... Kotsos, A. (2013). The use of digital image correlation for non-destructive and
864 multi-scale damage quantification. In *Sensors and smart structures technologies for*
865 *civil, mechanical, and aerospace systems 2013* (Vol. 8692, p. 86922H).
- 866 Shirole, D., Hedayat, A., & Walton, G. (2019). Experimental relationship between com-
867 pressional wave attenuation and surface strains in brittle rock. *Journal of Geophysical*
868 *Research: Solid Earth*, *124*(6), 5770–5793.
- 869 Shirole, D., Hedayat, A., & Walton, G. (2020). Illumination of damage in intact rocks by

- 870 ultrasonic transmission-reflection and digital image correlation. *Journal of Geophysical*
871 *Research: Solid Earth*, 125(7), e2020JB019526.
- 872 Shirole, D., Walton, G., & Hedayat, A. (2020). Experimental investigation of multi-scale
873 strain-field heterogeneity in rocks. *International Journal of Rock Mechanics and Min-*
874 *ing Sciences*, 127, 104212.
- 875 Sinha, S., Shirole, D., & Walton, G. (2020). Investigation of the micromechanical damage
876 process in a granitic rock using an inelastic bonded block model (bbm). *Journal of*
877 *Geophysical Research: Solid Earth*, 125(3), e2019JB018844.
- 878 Sondergeld, C., & Estey, L. (1982). Source mechanisms and microfracturing during uniaxial
879 cycling of rock. *pure and applied geophysics*, 120(1), 151–166.
- 880 Song, H., Zhang, H., Fu, D., Kang, Y., Huang, G., Qu, C., & Cai, Z. (2013). Experimental
881 study on damage evolution of rock under uniform and concentrated loading condi-
882 tions using digital image correlation. *Fatigue & Fracture of Engineering Materials &*
883 *Structures*, 36(8), 760–768.
- 884 Stacey, T. (1981). A simple extension strain criterion for fracture of brittle rock. In
885 *International journal of rock mechanics and mining sciences & geomechanics abstracts*
886 (Vol. 18, pp. 469–474).
- 887 Sutton, M. A., Orteu, J. J., & Schreier, H. (2009). *Image correlation for shape, motion and*
888 *deformation measurements: basic concepts, theory and applications*. Springer Science
889 & Business Media.
- 890 Tal, Y., Evans, B., & Mok, U. (2016). Direct observations of damage during unconfined
891 brittle failure of carrara marble. *Journal of Geophysical Research: Solid Earth*, 121(3),
892 1584–1609.
- 893 Tapponnier, P., & Brace, W. (1976). Development of stress-induced microcracks in westerly
894 granite. In *International journal of rock mechanics and mining sciences & geomechan-*
895 *ics abstracts* (Vol. 13, pp. 103–112).
- 896 Tarokh, A., Makhnenko, R. Y., Fakhimi, A., & Labuz, J. F. (2017). Scaling of the fracture
897 process zone in rock. *International Journal of Fracture*, 204(2), 191–204.
- 898 Wawersik, W., & Fairhurst, C. (1970). A study of brittle rock fracture in laboratory com-
899 pression experiments. In *International journal of rock mechanics and mining sciences*
900 *& geomechanics abstracts* (Vol. 7, pp. 561–575).
- 901 Wong, L., & Einstein, H. (2009). Crack coalescence in molded gypsum and carrara mar-
902 ble: part 2—microscopic observations and interpretation. *Rock Mechanics and Rock*
903 *Engineering*, 42(3), 513–545.
- 904 Wong, L. N. Y., & Xiong, Q. (2018). A method for multiscale interpretation of fracture pro-
905 cesses in carrara marble specimen containing a single flaw under uniaxial compression.
906 *Journal of Geophysical Research: Solid Earth*, 123(8), 6459–6490.
- 907 Wulff, A.-M., Hashida, T., Watanabe, K., & Takahashi, H. (1999). Attenuation behaviour
908 of tuffaceous sandstone and granite during microfracturing. *Geophysical Journal In-*
909 *ternational*, 139(2), 395–409.
- 910 Xu, X., & Zhang, Z.-Z. (2018). Acoustic emission and damage characteristics of granite
911 subjected to high temperature. *Advances in Materials Science and Engineering*, 2018.
- 912 Zafar, S., Hedayat, A., & Moradian, O. (2020). Evaluation of crack initiation and dam-
913 age in intact barre granite rocks using acoustic emission. *Geotechnical Earthquake*
914 *Engineering and Special Topics*.
- 915 Zhao, Y.-h., Huang, J.-f., & Wang, R. (1993). Real-time sem observations of the microfrac-
916 turing process in rock during a compression test. In *International journal of rock*
917 *mechanics and mining sciences & geomechanics abstracts* (Vol. 30, pp. 643–652).